

Joint full-waveform ground-penetrating radar and electrical resistivity inversion applied to field data acquired on the surface

Diego Domenzain¹, John Bradford¹, and Jodi Mead²

ABSTRACT

We exploit the different but complementary data sensitivities of ground-penetrating radar (GPR) and electrical resistivity (ER) by applying a multiphysics, multiparameter, simultaneous 2.5D joint inversion without invoking petrophysical relationships. Our method joins full-waveform inversion (FWI) GPR with adjoint derived ER sensitivities on the same computational domain. We incorporate a stable source estimation routine into the FWI-GPR. We apply our method in a controlled alluvial aquifer using only surface-acquired data. The site exhibits a shallow groundwater boundary and unconsolidated heterogeneous alluvial deposits. We compare our recovered parameters to individual FWI-GPR and ER results, and we compare them to log measurements of capacitive conductivity and neutron-derived porosity. Our joint inversion provides a more representative depiction of subsurface structures because it incorporates multiple intrinsic parameters, and it is therefore superior to an interpretation based on log data, FWI-GPR, or ER alone.

INTRODUCTION

Accurately quantifying electrical properties of the subsurface is a useful tool for soil characterization (Kaufmann et al., 2020), carbon dioxide monitoring (Carrigan et al., 2013), geothermal exploration (Spichak and Zakharova, 2015), contaminant detection (Babcock and Bradford, 2015), and groundwater quantity estimation (Parsekian et al., 2012; Beff et al., 2013). As our need to responsibly exploit natural resources grows ever more dire, so does our need to increase the resolution of our estimated subsurface parameters.

Time-domain ground-penetrating radar (GPR) is sensitive to electrical permittivity through reflectivity and velocity and to electrical conductivity through reflectivity and intrinsic attenuation. Full-waveform inversion (FWI) (Tarantola, 1984; Ernst et al., 2007a; Meles et al., 2010, 2012; Klotzsche et al., 2014) aims to recover subsurface parameters using the entire time-domain response of GPR data in a deterministic and physics driven way, therefore making full use of the information content of the GPR data. We note that other approaches exist that use the entire surface-acquired GPR waveform record to recover subsurface parameters. Busch et al. (2012) perform a gradient-free optimization of electrical parameters assuming a 3D horizontally layered subsurface. Liu et al. (2018) use stochastic optimization to find the size of a known object buried in a homogeneous half-space. For the entirety of this work, we refer to the term FWI in the context of Tarantola (1984) and Ernst et al. (2007b), i.e., computing the data sensitivities using the adjoint method.

In contrast to seismic wave propagation, many GPR applications exhibit electromagnetic velocities decreasing with depth, which hamper the sensitivity of the data at long offsets, which in turn challenge the low spatial-frequency content requirements for FWI with surface-acquired data (Virieux and Operto, 2009). Although FWI-GPR has been subject to a steady increase of interest over the past few years, most field data applications have focused on borehole GPR. See Klotzsche et al. (2019) for a review of current methods.

Steady-state electrical resistivity (ER) is directly sensitive to electrical conductivity. Moreover, the spatial-frequency content of the ER data is of a longer wavelength when compared with the GPR data. Domenzain et al. (2020b) circumvent the inherent issues of surface-acquired FWI-GPR by incorporating ER data in a simultaneous, multiparameter joint inversion that explicitly joins the FWI-GPR and ER data sensitivities. Domenzain et al. (2020a) expand this method by incorporating the envelope transform of the GPR data into the inversion and by using the cross-gradient constraint to enforce structural similarities. Moreover, the cross-gradient

Manuscript received by the Editor 8 March 2021; revised manuscript received 9 September 2021; published ahead of production 11 October 2021; published online 18 November 2021.

¹Colorado School of Mines, Golden, Colorado 78713-8924, USA. E-mail: diegodomenzain@mines.edu (corresponding author); jbradford@mines.edu.

²Boise State University, Boise, Idaho 83725, USA. E-mail: jmead@boisestate.edu.

© 2022 Society of Exploration Geophysicists. All rights reserved.

constraint is implemented by a decoupled optimization scheme that allows for different confidence weights on either the permittivity or conductivity solution.

Here, we present an example of joint inversion (Domenzain et al., 2020a) using FWI-GPR and ER surface-acquired field data collected at the Boise Hydrogeophysical Research Site (BHRS) (Barash et al., 1999). Given its shallow water table and density of wells, the BHRS has been used for benchmarking near-surface electromagnetic data acquisition methods (Mwenifumbo et al., 2009) and subsurface parameter inversion schemes (Ernst et al., 2007a; Irving et al., 2007; Oldenborger et al., 2007). We use previous GPR multioffset subsurface parameter estimations (Ernst et al., 2007a; Bradford et al., 2009) and logs of neutron-derived porosity and capacitive conductivity (Barrash and Clemo, 2002; Mwenifumbo et al., 2009) to compare our recovered parameters. Given that accurate initial models are needed for successful FWI results (Virieux and Operto, 2009), we use an initial velocity model obtained by a ray-based tomography approach from a previous GPR survey at the same site (Bradford et al., 2009). Finally, our joint inversion is free from petrophysical assumptions; hence, we do not incorporate any of the log measurements in our inversion schemes.

Because the method by Domenzain et al. (2020a) is presented for synthetic 2D data, we account for the 3D nature of field data by transforming the 3D GPR data onto two dimensions (Bleistein, 1986; Ernst et al., 2007a) and computing the 2.5D ER sensitivities directly from the 3D observed data (Domenzain et al., 2021). This way, the recovered parameters in our inversion are 2.5D, which coincides with the first-order features of the site geometry (Bradford et al., 2009). Notably, the 2.5D ER inversion algorithm is capable of efficiently handling (in memory and operation count) the very fine discretization constraints required by the FWI-GPR forward model (Courant et al., 1967). This enables direct comparison of the FWI-GPR and ER sensitivities without the need to interpolate the computational domain.

On average over all of the boreholes, we find that our joint recovered parameters outperform independent GPR or ER inversions when compared to the control log data. Notably, our joint recovered conductivity is a better structural match to the log porosity and capacitive conductivity than they are to each other. Our joint recovered permittivity and conductivity show features with a higher resolution than those of just the GPR and ER recovered parameters. Our method enhances the resolution of subsurface electrical parameters beyond the sensitivities of individual GPR and ER inversions.

To the authors' best knowledge, the work presented here is the first surface-acquired FWI (i.e., using the adjoint method for computing the data sensitivities) of field GPR data. Moreover, it is the first multiphysics electromagnetic inversion of field data directly joining sensitivities (i.e., without interpolating) from two methods that share the same parameter (i.e., electrical conductivity).

METHODS

Forward models

We consider 2D (Domenzain et al., 2020b) and 2.5D (Domenzain et al., 2021) forward models for the FWI-GPR and ER experiments, respectively. Both forward models assume 2.5D isotropic physics and 2D model parameters in the xz -plane; i.e., the model parameters exhibit negligible variation along the y -direction. We assume the

GPR and ER 2D conductivity to be equal. Enabled by the efficient 2.5D ER inversion routine by Domenzain et al. (2021), both forward models are discretized on the same computational grid.

We note that the transverse-electric (TE) GPR forward model is implemented in a staggered grid. This means that the source forcing is given in terms of current density (J_y) and not electric field (E_y). In what follows, we refer to the relative electrical permittivity (i.e., ϵ_r) only by permittivity and to the electrical conductivity only by conductivity (σ). Bold letters will denote the discrete version of their continuous counterpart. We denote by $\mathbf{d}_w^{o,s}$ (and $\mathbf{d}_{dc}^{o,s}$) the observed GPR (and ER) data for each shot gather (and source-sink pair). The superscript s denotes data from a single shot gather (for GPR) or a single source-sink pair (for ER). The superscript o refers to the observed data, and when it is omitted we refer to synthetic data. The discrete source term for the GPR forward model is denoted as \mathbf{s}_w .

Our full-waveform GPR forward model assumes certain limitations of the underlying physics. First, the subsurface parameters are assumed to be frequency-independent. However, as noted by Annan (1996) and Bradford (2006), this approximation is reasonable for most subsurface permittivity values over the frequency band of a typical GPR wavelet. Concerning conductivity, most earth materials range in at most an order of magnitude between DC and frequency-dependent conductivity (Domenzain et al., 2020b); hence, we assume that this approximation is also valid. Second, we do not model the 3D radiation pattern of the GPR antenna because our source term is modeled as an infinite dipole line source in the y -direction. However, the 2D approximation is reasonable for the TE mode (Bradford, 2012), which is the case presented here. Finally, we approximately correct for 3D wavefield spreading using the approach by Bleistein (1986), which transforms the 3D data record to a 2D data record.

We recognize that the 2D GPR data transform as given by Bleistein (1986) is asymptotic, does not correct for out-of-plane events, does not consider intrinsic attenuation (governed by conductivity in the case of GPR), is only valid in the far-field, and explicitly assumes known and continuous velocities in the subsurface. Despite these limitations, much of the literature on field data FWI-GPR (see Klotzsche et al., 2019) uses this transform. This is mostly due to the present-day computational burden of applying a full 3D forward model. For example, Mozaffari et al. (2020) perform a 2.5D FWI-GPR using a 3D forward model. Synthetically, they show that, when no sharp velocity contrasts are present in the subsurface, the average model errors are improved by 2% when compared to a 2D FWI-GPR. In the case of sharp velocity contrasts, the improvement is 20%. However, they mention that their computational cost increases by 300%. Given the present burden of computational time versus improvement, we choose to use a 2D FWI-GPR approach.

Data preprocessing

Certain preprocessing steps need to be applied to our data before we perform our joint inversion. Most notably for GPR, these steps ensure the physical accuracy and numerical stability of the forward model.

GPR preprocessing

We remove the wow (Annan, 1996) and higher time-frequency noise with a frequency-domain Gaussian band-pass filter. As explained in the “GPR source estimation” subsection, further

refinement of the time-frequency content of the data might be needed to ensure that the FWI source inversion routine is stable.

Because our data were acquired in three dimensions and our forward model is in two dimensions, we transform our GPR data to a 2D wave record using the approach by Bleistein (1986). This method requires a reference constant velocity v_o as input. As mentioned by Bleistein (1986), Ernst et al. (2007a), and Klotzsche et al. (2019), the choice for v_o is arbitrary and it is often taken as the most representative velocity in the subsurface.

The next step is to ensure that our forward model can numerically handle our observed data. We apply the condition given by Courant et al. (1967) and use the range of velocities from the most coherent events in linear and hyperbolic velocity semblances. The maximum frequency is chosen slightly larger than the band-pass filter used on the observed data. This ensures that our forward model has enough room to capture smaller wavelengths that might arise in the inversion.

Given our target velocities and maximum frequency, the time sampling given by the instrument is too large for our numerical scheme. We use Fourier interpolation to finely sample our GPR observed data to the required time sampling. We note that choosing the maximum frequency and target velocities determines the discretization grid size in time and space. In our joint inversion, FWI-GPR and ER forward models share the same discretization of the spatial model parameters. Therefore, the range of target velocities and frequency content determines the entire computational domain.

The last step is to remove unwanted receiver traces. Short- and long-offset traces are removed if early amplitudes are clipped or if no meaningful reflections are observed at late times. We list these preprocessing steps as follows for easy reference. For each shot gather $\mathbf{d}_w^{o,s}$,

- 1) dewow $\mathbf{d}_w^{o,s}$
- 2) band-pass $\mathbf{d}_w^{o,s}$ in time
- 3) apply 2.5D correction to $\mathbf{d}_w^{o,s}$
- 4) interpolate $\mathbf{d}_w^{o,s}$ in time
- 5) remove unwanted receivers in $\mathbf{d}_w^{o,s}$.

GPR source estimation

Using an appropriate source wavelet is an important step in FWI schemes. When dealing with field data, a common approach is to find a deconvolution filter (at each iteration of the FWI scheme) that matches the synthetic to the observed data and then use this filter on the current estimate of the source wavelet (Pratt et al., 1998; Ernst et al., 2007a; Groos et al., 2017). We find that this approach is stable when the initial source wavelet is already very similar in shape to the true source wavelet. Here, we present an approach to estimate the initial source wavelet (before the FWI-GPR routine) based only on the observed data and initial model parameters, which ensures the stability of the source inversion scheme by Pratt et al. (1998) (within the FWI-GPR routine) for our field data.

Our initial source wavelet estimation is done in three stages. The first stage captures a qualitative shape in time of the source wavelet. At this stage, all shot gathers have the same source wavelet. The second stage corrects individually for each shot gather the amplitude and small time-zero variations that are inherent in subsurface electrical parameters and the small inaccuracies of the instrument when triggering the shot. At this stage, each shot gather has a different source

wavelet. The third stage ensures the source inversion routine within the FWI-GPR to be stable. Once these three stages are complete, the joint inversion begins, and the source inversion scheme of Pratt et al. (1998) is applied at each iteration.

We now explain the first stage in detail. After applying the preprocessing steps on the observed data, we apply a linear moveout correction with a predefined velocity. We choose this velocity from the most coherent linear arrival in all shot gathers. We then vertically sum the traces to get an average source wavelet. We remove late-time events by applying a Gaussian mute \mathbf{g}^s in time around the event of interest. The next step is to time shift the wavelet and Gaussian mute to match when the shot was triggered. We use the velocity of the selected event and the source-receiver offset for this purpose. We repeat this process for all shot gathers. The end result is a source wavelet with a representative shape for all shot gathers with the correct time zero. This correction is correct up to our choice of velocity for the selected event. Here, we list the steps of this first stage:

- 1) apply preprocessing steps to $\mathbf{d}_w^{o,s}$
- 2) apply a linear moveout on $\mathbf{d}_w^{o,s}$ and stack to get \mathbf{s}_w^s
- 3) apply the Gaussian mute \mathbf{g}^s on \mathbf{s}_w^s :

$$\mathbf{s}_w^s \leftarrow \mathbf{g}^s \odot \mathbf{s}_w^s \quad (1)$$

- 4) shift \mathbf{s}_w^s and \mathbf{g}^s to match when shot was triggered
- 5) repeat steps 1–4 and collect \mathbf{s}_w^s and \mathbf{g}^s for all shots
- 6) average all \mathbf{s}_w^s and \mathbf{g}^s to get \mathbf{s}_w and \mathbf{g}
- 7) get \mathbf{s}_w in terms of current density:

$$\mathbf{s}_w \leftarrow - \int_0^T \mathbf{s}_w dt \quad (2)$$

- 8) apply \mathbf{g} on \mathbf{s}_w :

$$\mathbf{s}_w \leftarrow \mathbf{g} \odot \mathbf{s}_w. \quad (3)$$

Because of subsurface parameter variations along the survey line, not all source wavelet estimates will be equal in shape for all shot gathers. To remove these slight variations, we average all source estimates and all Gaussian mutes over all shot gathers. We interpret the resulting source wavelet \mathbf{s}_w as having an approximate but representative shape in time for all shot gathers. At this point, the true amplitude of the source wavelet is not important. Here, the source estimate is a qualitative average of the electric field E_y and not of the current density J_y . The next step in the first stage is to numerically integrate the source wavelet to obtain a qualitative estimate of current density:

$$\mathbf{s}_w \leftarrow - \int_0^T \mathbf{s}_w dt, \quad (4)$$

where T denotes the total time recorded in the data. The constant of integration is set to zero because we assume a zero-mean wavefield. Finally, we apply the average Gaussian \mathbf{g} mute to \mathbf{s}_w .

We now explain in detail the second stage. Due to subsurface variations and small inaccuracies of the GPR instrument, the input power as well as the time when the shot was triggered vary for each

shot gather. We correct for these inaccuracies by comparing the synthetic and observed data. At this point, only an initial estimate for subsurface parameters is needed, for example, a homogeneous conductivity and a reflection-tomography permittivity model.

The first step for stage two is to compute the amount by which to scale the amplitude of the first arrival in the first receiver trace of the synthetic data to the observed data. We store these amplitude-matching ratios for all shot gathers. Because our initial subsurface parameters are not correct, these amplitude-matching ratios are not exact. Therefore, we apply a window average on the collected ratios and apply these averaged amplitude corrections to each source estimate for each shot gather. We find that a window length of 25% of the total number of shot gathers is enough. Finally, we shift the source wavelet in time by the amount needed to match the first arrival of the first receiver trace of the synthetic data to the observed data. We list the steps of this second stage in the following list:

- 1) Compute synthetic data \mathbf{d}_w^s with initial models and first source estimate \mathbf{s}_w .
- 2) Using \mathbf{s}_w and the first receiver trace of $\mathbf{d}_w^{o,s}$ and \mathbf{d}_w^s
 - obtain \mathbf{s}_w^s for each shot gather by correcting the amplitude of \mathbf{s}_w
 - shift \mathbf{s}_w^s in time to match when the shot was triggered
 - shift \mathbf{g} by same amount to obtain \mathbf{g}^s .
- 3) Repeat steps 1 and 2 for all shots.

We now explain in detail the third stage. The purpose for this stage is to correct the frequency content in our observed data in order for the source wavelet inversion within the FWI-GPR to be stable. This is similar to the approach by Busch et al. (2012), who remove offset-frequency pairs from each shot gather that are smaller than a given threshold computed from the data. Our approach computes an equivalent of this threshold by comparing the estimated source wavelet to the observed data.

The first step of stage three is to compute the update of the source inversion scheme by Pratt et al. (1998). This approach applies a Wiener filter \mathbf{a}^s (that matches \mathbf{d}_w^s to $\mathbf{d}_w^{o,s}$) on the source estimate \mathbf{s}_w^s . Because our data are expressed in terms of an electric field, we transform \mathbf{s}_w^s from current density to electric field

$$\mathbf{s}_w^s \leftarrow -\dot{\mathbf{s}}_w^s. \quad (5)$$

Then, for each frequency f and all receivers, we compute the filter \mathbf{a}^s in the frequency domain by

$$\hat{\mathbf{a}}^s(f) = \frac{\hat{\mathbf{d}}_w^{o,s}(f) \cdot \hat{\mathbf{d}}_w^{s,\dagger}(f)}{\hat{\mathbf{d}}_w^s(f) \cdot \hat{\mathbf{d}}_w^{s,\dagger}(f) + \eta}, \quad (6)$$

where \cdot denotes the dot product, the hat symbol $\hat{\cdot}$ denotes the frequency-domain representation, \dagger denotes the conjugate transpose, and η is a small fixed real number that regularizes $\hat{\mathbf{a}}^s$. We choose $\eta = 10^{-10}$. The next step is to apply this filter to our source estimate,

$$\hat{\mathbf{s}}_w^s \leftarrow \hat{\mathbf{s}}_w^s \odot \hat{\mathbf{a}}^s, \quad (7)$$

and then we transform our new source estimate back to the time domain. The new source estimate \mathbf{s}_w^s is in terms of the electric

field, so we numerically integrate \mathbf{s}_w^s using equation 4 to have the expression in terms of current density.

Stage three aims to determine the final frequency content of our observed data. After stage two, the spectral content of the source wavelet might contain higher frequencies than the (band-pass filtered) observed data. Our experience shows that these oscillations can render the source inversion within the FWI-GPR scheme unstable. If this is the case, we apply a more aggressive low-pass filter to all $\mathbf{d}_w^{o,s}$, compute our forward model again, and repeat equations 4, 5, and 7, until the frequency content of \mathbf{s}_w^s lies within that of $\mathbf{d}_w^{o,s}$. We list the steps of this third stage in the following list:

- 1) compute synthetic data \mathbf{d}_w^s with initial models and second source estimate \mathbf{s}_w^s
- 2) transform \mathbf{s}_w^s to the electric field,

$$\mathbf{s}_w^s \leftarrow -\dot{\mathbf{s}}_w^s \quad (8)$$

- 3) compute the Wiener filter $\hat{\mathbf{a}}^s$ using \mathbf{s}_w^s , $\mathbf{d}_w^{o,s}$, and \mathbf{d}_w^s ,

$$\hat{\mathbf{s}}_w^s \leftarrow \hat{\mathbf{s}}_w^s \odot \hat{\mathbf{a}}^s \quad (9)$$

- 4) if \mathbf{s}_w^s has larger frequency content than the previous wavelet, low-pass filter $\mathbf{d}_w^{o,s}$ and repeat from the second GPR source estimation stage
- 5) transform \mathbf{s}_w^s back to current density,

$$\mathbf{s}_w^s \leftarrow -\int_0^T \mathbf{s}_w^s dt \quad (10)$$

- 6) apply mute \mathbf{g}^s to \mathbf{s}_w^s
- 7) repeat 1–6 for all shots.

As an example, consider \mathbf{s}_w^s as shown in Figure 1a after the second stage for a given shot gather. Figure 1b shows \mathbf{s}_w^s after step 5 of stage three for the same shot gather. We note that short period oscillations have been introduced when compared with Figure 1a. Figure 1c shows the Wiener recovered source after the observed data were more aggressively low-pass filtered.

The last step of stage three is to mute the Wiener recovered wavelet \mathbf{s}_w^s with the Gaussian mute in time \mathbf{g}^s from stage two. As noted by Pratt et al. (1998), this step is necessary to remove late reflection events in the source wavelet. Moreover, because the Wiener filter is not exact, this step ensures causality.

Once these three stages are complete, the joint inversion begins and the source estimation scheme by Pratt et al. (1998) is implemented at each iteration. This source estimation scheme is the same as stage three without implementing step 4.

ER preprocessing

First, we remove all values in \mathbf{d}_{dc}^o whose apparent resistivities are negative. These values are not physical and are contaminated by noise. Then, we remove all data points whose standard deviation is larger than a fixed cutoff. Finally, to model multireceiver pairs for a single source-sink position, we divide each voltage value in \mathbf{d}_{dc}^o by the electrical current magnitude given by the instrument. We list these steps in the following list for easy reference:

- 1) remove negative apparent resistivities from \mathbf{d}_{dc}^o
- 2) eliminate elements of \mathbf{d}_{dc}^o whose standard deviation is more than a fixed cutoff
- 3) divide each element of \mathbf{d}_{dc}^o by their respective source current magnitude.

Once these steps have been completed, we take the average of the apparent resistivities among all of the data. We use the multiplicative inverse of this value for the initial homogeneous conductivity.

Joint inversion

The purpose of our joint inversion is to find positive 2D $\boldsymbol{\varepsilon}_r$ and $\boldsymbol{\sigma}_*$ such that

$$\{\boldsymbol{\varepsilon}_{r*}, \boldsymbol{\sigma}_*\} = \arg \min \tilde{\Theta}_w(\boldsymbol{\varepsilon}_r, \boldsymbol{\sigma}; \mathbf{d}_w^o, \mathbf{d}_{w,a}^o) + \Theta_{dc}(\boldsymbol{\sigma}; \mathbf{d}_{dc}^o) + \Theta_\tau(\boldsymbol{\varepsilon}_r, \boldsymbol{\sigma}), \quad (11)$$

where the root-mean square (rms) of the FWI-GPR data and its envelope ($\mathbf{d}_{w,a}^o$) is denoted by $\tilde{\Theta}_w$, the ER data rms is given by Θ_{dc} , and the cross-gradient constraint by Θ_τ . The tilde on $\tilde{\Theta}_w$ denotes the use of the GPR data and its envelope. As mentioned in the ‘‘Forward models’’ subsection, we assume that the DC and GPR conductivity are equal. Domenzain et al. (2020a) explain in detail each term in equation 11.

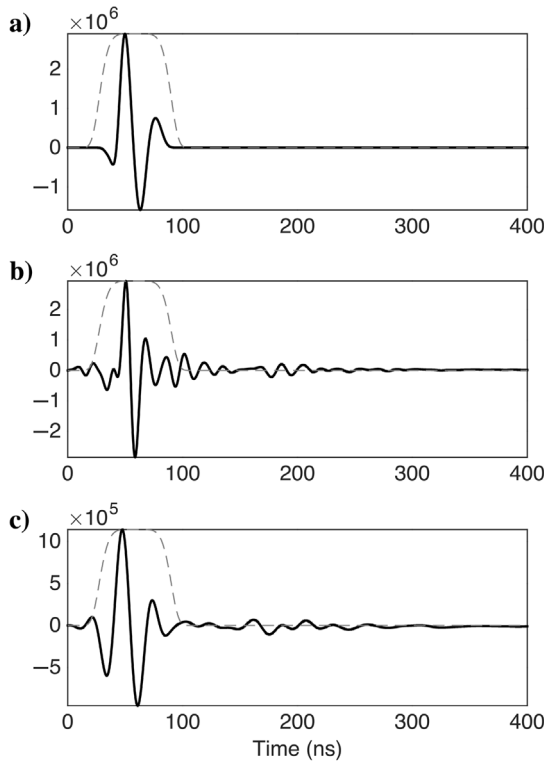


Figure 1. (a) Source estimates for shot gather 1 as given by stage 2, (b) after applying the Wiener filter with the observed data band-pass filtered between 10 and 100 MHz, and (c) between 10 and 50 MHz. The Gaussian mute is shown (but not applied) in dashed gray. Amplitudes are in units of current density (A/m^2). The frequency-domain plots of (b and c) are shown in Figure 10a and 10b, respectively.

The minimization of equation 11 is performed by a nonlinear multiparameter optimization method that computes the gradients of $\tilde{\Theta}_w$ and Θ_{dc} using the adjoint method for the GPR and ER data (commonly referred to as FWI in the GPR case). Domenzain et al. (2020a) present a solution of equation 11 for 2D synthetic data. This optimization is performed jointly in the sense that all terms being summed in equation 11 influence the updates of $\boldsymbol{\varepsilon}_r$ and $\boldsymbol{\sigma}$ at all iterations. This means that we do not use either $\boldsymbol{\varepsilon}_r$ or $\boldsymbol{\sigma}$ as reference parameters for each other. Rather, we solve for them together in the inversion process. Moreover, $\boldsymbol{\varepsilon}_r$ and $\boldsymbol{\sigma}$ are discretized on the same computational domain, so no interpolation is needed. Aside from good initial $\boldsymbol{\varepsilon}_r$ and $\boldsymbol{\sigma}$ models, we do not regularize our inversion.

At each iteration of the inversion, the different updates of $\tilde{\Theta}_w$, Θ_{dc} , and Θ_τ are joined together by an ad hoc weighting scheme with variable coefficients. This scheme accounts for the different sensitivities of the FWI-GPR and ER data and enables different weighting strategies depending on whether the data are most sensitive to $\boldsymbol{\varepsilon}_r$ or $\boldsymbol{\sigma}$. A detailed review is found in Domenzain et al. (2020b, 2020a). Here, we present a condensed explanation of each weight.

Let $\Delta\boldsymbol{\sigma}_{w,\sigma}$ and $\Delta\boldsymbol{\sigma}_{dc}$ denote the FWI-GPR and ER sensitivities, respectively, that result from optimizing $\tilde{\Theta}_w$ and Θ_{dc} at each iteration. The conductivity sensitivity with which we update $\boldsymbol{\sigma}$ at each iteration is given by $\Delta\boldsymbol{\sigma}$:

$$\Delta\boldsymbol{\sigma} = a_{dc}\Delta\boldsymbol{\sigma}_{dc} + a_w\Delta\boldsymbol{\sigma}_{w,\sigma}, \quad (12)$$

where a_{dc} and a_w follow the approximate shape over the iterations given in Figure 2a. The decoupled cross-gradient constraint on $\boldsymbol{\varepsilon}_r$ and $\boldsymbol{\sigma}$ is enforced by the weights $b_{\boldsymbol{\varepsilon}_r}$ and b_σ , respectively (see Figure 2b).

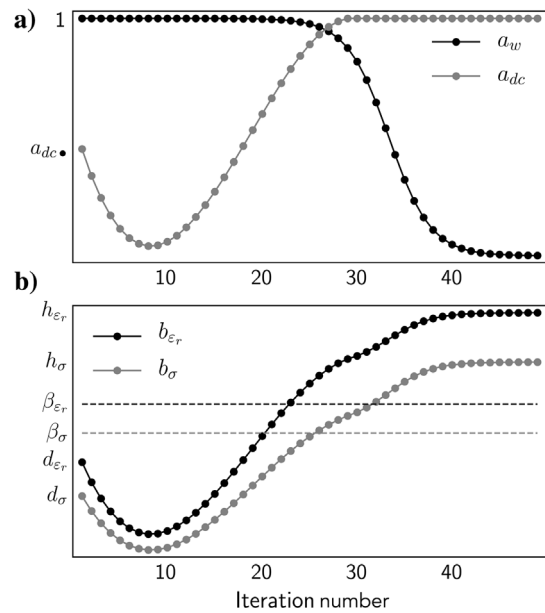


Figure 2. Qualitative shape of weights during the inversion. On the y-axis, constant hyperparameters chosen before the inversion. Plotted, the variable weights used throughout the inversion as a function of iterations. (a) The weights used to join the FWI-GPR and ER conductivity sensitivities. (b) The weights used to join the cross-gradient constraints ($b_{\boldsymbol{\varepsilon}_r}$ and b_σ) and the envelope gradients ($\beta_{\boldsymbol{\varepsilon}_r}$ and β_σ).

Finally, the envelope sensitivities are weighted by the constant real numbers β_{ϵ_r} and β_{σ} .

In practice, at each iteration, the weights a_{dc} , a_w , b_{ϵ_r} , and b_{σ} are computed as a function of the values of $\tilde{\Theta}_w$, Θ_{dc} and 12 constant hyperparameters that are chosen before the inversion. Table 1 shows these hyperparameters and their purpose in the inversion. In Appendix B, we explain how we found these hyperparameters for our field data.

Mathematically, our weighting scheme for $\Delta\sigma_{dc}$ and $\Delta\sigma_{w,\sigma}$ as a function of $\tilde{\Theta}_w$ and Θ_{dc} is motivated by two objectives: (1) enabling the inversion to comply with the GPR and ER descent directions and simultaneously (2) finding a good fit for the GPR and ER data. Physically (assuming the approximation that the DC and GPR conductivity are equal [Domenzain et al., 2020b]), these two objectives translate to obtaining a conductivity solution that (1) complies with GPR and ER data and (2) does not favor a better fit of either GPR or ER data.

These two objectives together enable the joint inversion to overcome the local minima present in GPR and ER stand-alone inversions. To achieve these objectives, the joint inversion should not start with the conductivity solution recovered by a stand-alone ER inversion. If this was the case, then such a solution would already be a local minima of Θ_{dc} and $\Delta\sigma_{dc}$ would hold no relevant information for either the GPR or ER descent direction.

Because at early iterations the solutions σ and ϵ_r give a poor fit to the data, their structural information is not well resolved. However, at late iterations, we expect these solutions to be better resolved; hence, their structural information is closer to the true models. The weights β_{ϵ_r} and β_{σ} exploit this observation as shown in Figure 2b.

To apply this method to our field data case, we make two modifications. First, the ER sensitivities are computed using a 2.5D inversion scheme as explained by Domenzain et al. (2021). Second, at each iteration, the joint conductivity update $\Delta\sigma$ is multiplied by a fixed real number α_{σ} :

$$\Delta\sigma \leftarrow \alpha_{\sigma} \Delta\sigma. \quad (13)$$

Table 1. Hyperparameter values and their purpose in our joint inversion scheme.

Weight	Purpose	Value
a_{dc}	Initial weight on $\Delta\sigma_{dc}$	0.9
\dot{a}_{dc}	Steepness rise of a_{dc}	2
$\dot{\Theta}_{dc}$	Increase in a_{dc} if Θ_{dc} increases	4
\dot{a}_w	Steepness in decrease of a_w	10
$\dot{\Theta}_{w,\sigma}$	Increase in a_w if Θ_w increases	0.9
d_{ϵ_r}	Initial value of b_{ϵ_r}	10^{-4}
h_{ϵ_r}	Asymptotic value of b_{ϵ_r}	10^{-3}
d_{σ}	Initial value of b_{σ}	10^{-4}
h_{σ}	Asymptotic value of b_{σ}	10^{-3}
β_{ϵ_r}	Constant value for the envelope gradient of ϵ_r	5×10^{-3}
β_{σ}	Constant value for the envelope gradient of σ	10^{-3}
α_{dc}	Final step size for $\Delta\sigma$	2

The first modification results in a more accurate physical model because the nature of our field data is 3D and assumed 2.5D. The second modification is inherent to the observed data. We find that the sensitivity of the observed GPR data to conductivity is very poor; therefore, we use a fixed real number $\alpha_{\sigma} \geq 1$ to speed up the convergence of the overall scheme.

Figure 3 shows the workflow for the field data joint inversion scheme including the data preprocessing steps. The joint inversion is done following Domenzain et al. (2020a) with the two modifications noted previously.

FIELD SITE

The BHRS (Figure 4) is a research well field located on a gravel bar adjacent to the Boise River 15 km from Boise, Idaho, USA, and it is downstream of a nearby irrigation dam that controls the flux of the river throughout the year. The aquifer consists of coarse (cobble and sand) fluvial deposits overlaying clay. Stratigraphic units in the aquifer include an upper sand channel that thickens toward the river and pinches out in the middle of the well field, four underlying cobble-dominated units that alternate in relative porosity (i.e., packing density), and the presence of local sandier lenses (Barrash and Clemo, 2002; Barrash and Reboulet, 2004). The shallow BHRS aquifer is unconfined with the water table being generally 0–2 m below the land surface depending on the seasonal river stage.

We chose BHRS because of its record of previous borehole geophysical experiments, including those of Ernst et al. (2007a), Bradford et al. (2009), and Klotzsche et al. (2014), who characterize the site using the multioffset borehole and surface-acquired GPR data,

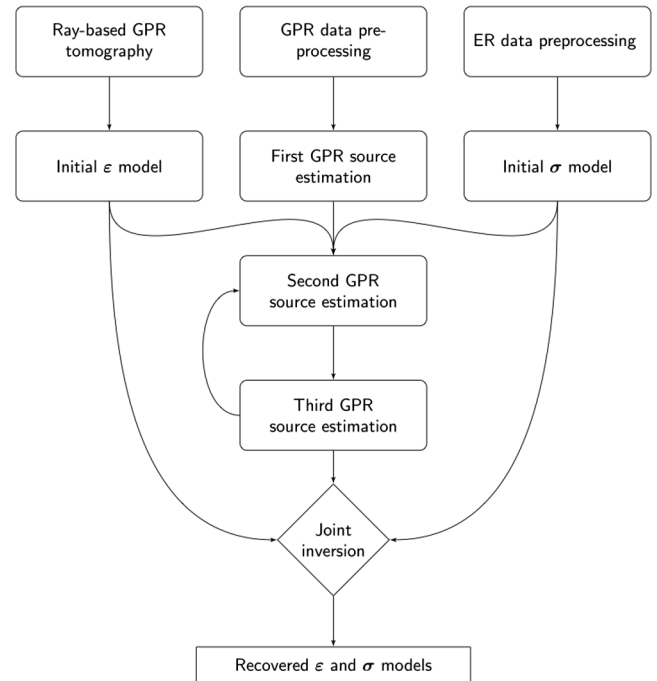


Figure 3. Joint inversion algorithm with preprocessing steps and GPR source wavelet estimation. Within the joint inversion, we estimate the source wavelet for each shot gather using the third GPR source estimation stage, except we omit step 4 of stage 3. The conductivity initial model is homogeneous with a value equal to the average observed apparent conductivities.

whereas Barrash and Clemo (2002), Mwenifumbo et al. (2009), and Barrash and Reboulet (2004) show neutron porosity logs, capacitive conductivity logs, and lithology from core, respectively, to detail the site stratigraphy and parameter distributions. We use these previous surveys as the context for and external verification of our recovered parameters.

Data acquisition

Based on previous knowledge of the site (Bradford et al., 2009), we assume that the subsurface presents a 2.5D geometry. Therefore, we position our survey line perpendicular to the strike of the primary sedimentary structure: a sand-filled erosional channel described as unit 5 by Barrash and Clemo (2002). The surface of the site has low topographic relief of 0.4 m over the 36 m survey line. Figure 4 shows our survey line and site wells, of which we only used B5, A1, and B2. The water table at the time of the survey was approximately 1 m below the ground surface at these wells. The GPR and ER experiments were performed during the same day and along the same survey line, but not at the same time (they were approximately 30 min apart).

GPR acquisition

We acquired multioffset GPR data with 50 MHz unshielded antennas on a Sensors & Software pulseEKKO Pro instrument. The antennas were positioned perpendicular to the survey line. Because the GPR equipment only consists of one transmitter-receiver pair, we acquire a single shot gather by leaving the transmitter antenna fixed and moving the receiver antenna along the line. At each source-receiver pair in our survey, the antenna positions are held fixed and a shot is performed. This procedure is repeated for all receivers and for all shots. Figure 5 shows the position for all of the shot-receiver pairs in our survey.

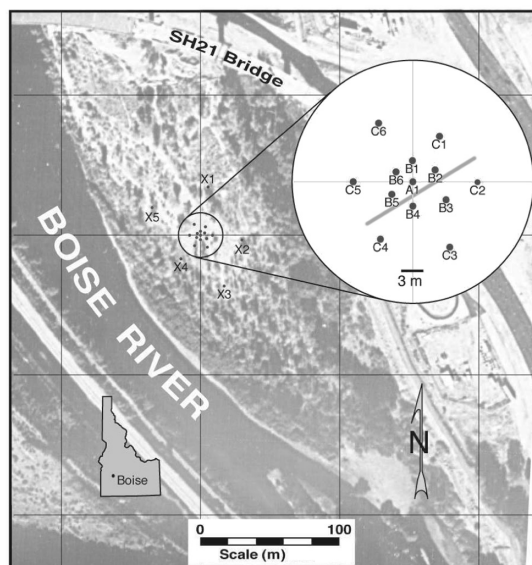


Figure 4. BHRS, located near Boise, Idaho, USA. Picture modified after Barrash et al. (1999). Existing borehole locations are marked with gray dots. A diagram of our GPR and ER survey line is marked in light gray.

The GPR receiver spacing is chosen to not spatially alias our data. Based on previous knowledge of the site (Bradford et al., 2009), the unsaturated layer has an electromagnetic velocity of approximately 0.15 m/ns. Given that our survey frequency was 50 MHz, we assume that this upper layer has a characteristic wavelength of approximately 3 m. Hence, we choose a receiver spacing of 0.5 m, which is one-third of the Nyquist minimum requirement for the considered parameters. The source spacing was 2 m, and the time sampling was 1 ns. The total recorded time was 700 ns. However, after 400 ns, the data hold no meaningful reflection events and have an amplitude equal to the noise level. In what follows, we assume that the GPR data only span to 400 ns for all shot gathers.

To increase our data sensitivity below the water table, we scheduled our experiments when the water table was at a very shallow depth, but without the site being flooded. Figure 6a shows the unprocessed GPR shot gather 1 as recorded by the instrument.

Given the depth to the unsaturated layer (approximately 1 m) and the characteristic wavelength in this layer (approximately 3 m), the resolution of the GPR data is limited in this shallow region. As explained in Appendix A, we built an initial velocity model using an additional GPR data set along the same line but performed at a different time when the water table was at a depth of approximately 2 m.

ER acquisition

The ER electrodes were placed along the same line as the GPR experiment, but at a separate moment in time. We used an IRIS Syscal Pro instrument with a total of 32 electrodes with 1 m spacing. All possible dipole-dipole and Wenner arrays were performed. Each source-receiver pair was repeated eight times, and a standard deviation value for each source-receiver pair was given by the instrument. Figure 5 shows the position of the electrodes in the survey.

GPR preprocessing

We follow the steps explained in the previous “GPR preprocessing” subsection. Short-offset traces that were clipped in the data were removed. As shown in Figure 5, the source-receiver offset varies slightly for each shot. This offset is on average approximately 7.5 m, which is more than double the estimate for the characteristic

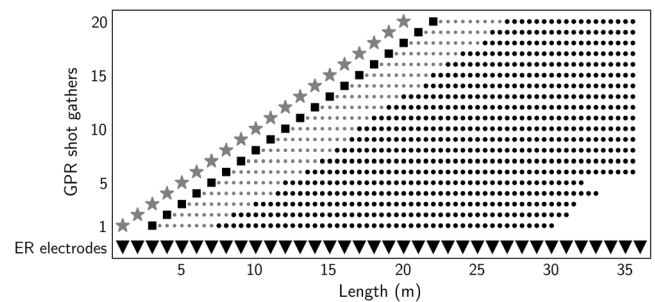


Figure 5. The GPR sources (the stars) and receivers (the solid circles) used in the inversion. Receiver positions measured in the field but discarded due to clipped early amplitudes are gray. The black squares indicate the common-offset gather we used to illustrate subsurface heterogeneity. In triangles, the ER electrodes. The zero meter mark is toward the river. Both surveys were done during the same day, but not at the same time.

wavelength at the near surface (approximately 3 m). Hence, in these data, removing short-offset traces serves two purposes: (1) signal quality control and (2) ensuring far-field data in the subsurface and, thus, a more accurate 2.5D transform at depth.

Figure 7 shows the average frequency spectra of all raw observed GPR data in black. The data were band-pass filtered between 10 and 100 MHz (see Figure 7 in the dark gray). We then perform the 2.5D

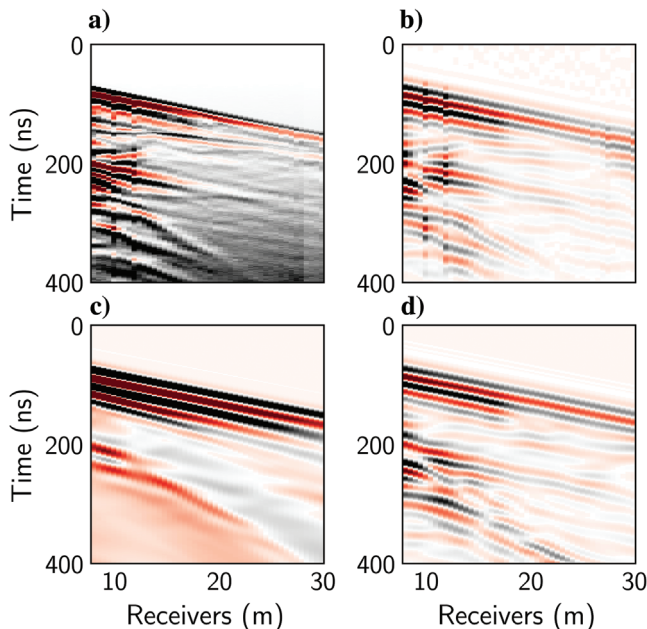


Figure 6. GPR shot gather 1. (a) Unprocessed (raw), (b) processed and ready for inversion (band-pass filtered between 10 and 50 MHz), (c) initial model, and (d) recovered using joint inversion. Time zero marks the beginning of our forward model, including a 30 ns delay to the start of the source wavelet. All amplitudes are gained in time by t^2 , and clipped to 50% of the maximum and minimum amplitude of the observed data. Amplitude zero is shown in the shade of gray at early times.

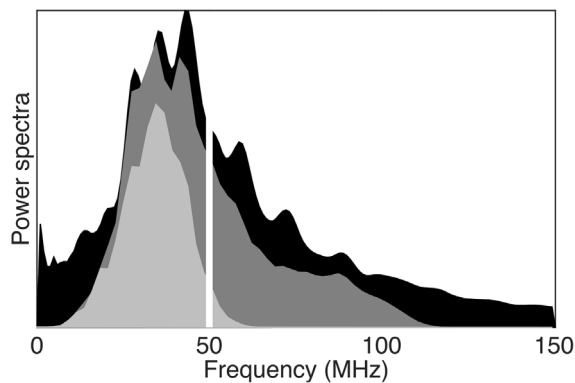


Figure 7. Average frequency content of our GPR data for all shot gathers. In black, the observed data. In dark gray, after the first band-pass applied to the observed data (10–100 MHz). In light gray, after the low-pass filter needed to ensure source inversion stability (50 MHz). In white, the central frequency of the GPR antenna in the field (50 MHz). Magnitudes are shown in linear scale and without normalization.

correction with $v_o = 0.13$ m/ns. Anticipating target velocities ranging from 0.06 to 0.3 m/ns, and a maximum frequency of 120 MHz, we choose the discretization parameters as summarized in Table 2.

Figure 6b shows shot gather 1 after all processing steps. In Figure 8a, we show the processed common-offset gather of the first receivers (see Figure 5). The time zero is the same as in Figure 6. An amplitude gain in time of t^2 was applied only for display purposes. Although we do not use these data for the inversion, we find it useful for interpreting the subsurface. For example, events *a*, *b*, and *c* show strong reflections, which are explained in detail in the “Inversions” section.

GPR source estimation

First, we complete stage one. For this particular data set, the only coherent linear event across all traces is the first-arrival air wave. We use this event to estimate the approximate source wavelet recognizing that the frequency content is not exactly equivalent to the signal traveling in the subsurface. Figure 9a shows source estimates for

Table 2. Discretization parameters used in our forward models.

$\Delta x, \Delta z$	0.05 m
Δt	0.1 ns
Air layer	3 m
Perfectly matched layers	1 m
Subsurface domain	45×15 m

The air and perfectly matched layers are not present in our ER forward model. The subsurface domain is the same for the GPR and ER forward models.

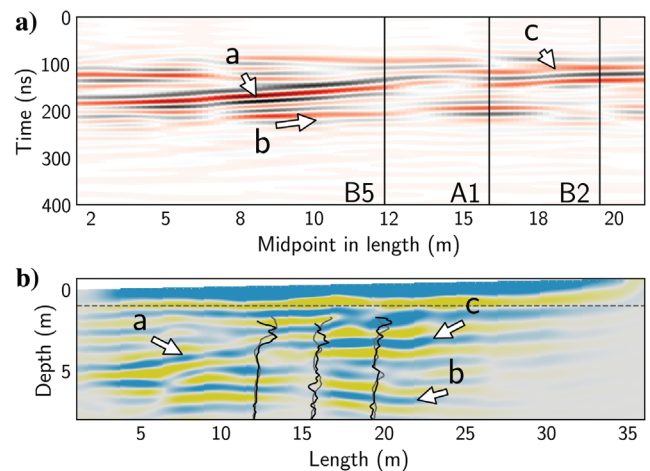


Figure 8. (a) Common-offset gather of the first receiver in our survey marked with borehole locations. The data were band-pass filtered between 10 and 50 MHz, and gained in time by t^2 . Time zero is when the shot was performed. (b) Reverse time migrated reflectivity of the GPR data computed with our joint inversion recovered parameters. Data profiles of capacitive conductivity (black) and porosity (gray) are overlaid at the log locations. The marked events *a*, *b*, and *c* (in both panels) correspond to the deep edge of the sand channel and reflectors at a depth of approximately 6 m and approximately 2.5 m, respectively.

each shot gather after step 5 of stage one in gray and the average source wavelet in black. Figure 9b shows the estimated source wavelet of section current density and the average Gaussian mute after this first stage.

We now begin stage two. For the initial models, conductivity is taken from the ER data (homogeneous value equal to the average of all of the observed apparent conductivities), and the permittivity is taken from the velocity estimation strategy outlined in Appendix A. Figure 9c shows the resulting sources for each shot gather after stage two is completed.

We now begin stage three. Figure 10a shows in black the power spectra of the electric field representation of s_w^s after the second stage for shot gather 1. In dark gray, we show the power spectra of the observed data for the same shot gather band-pass filtered between 10 and 100 MHz. In light gray, we show the power spectra of the electric field representation of the recovered s_w^s after applying the Wiener filter. Note that the frequency content of the Wiener recovered s_w^s has significantly deviated from that of our observed data.

We apply a low-pass filter to our observed data with a cutoff frequency of 50 MHz. The resulting power spectra are shown in dark gray in Figure 10b. This cutoff frequency is the highest frequency at which the filtered Wiener recovered s_w^s does not have frequencies larger than the source estimate from stage two.

We then repeat stage three. The power spectra of the new Wiener recovered source are shown in light gray in Figure 10b. Note that the power spectra of this new s_w^s (Figure 10b, light gray) resemble the observed data more than with the previous estimate. Moreover, the new power spectra of the observed data lies within the Wiener recovered source. The time domain representation of this stage can be found in Figure 1.

ER preprocessing

We follow the steps in the previous “ER preprocessing” subsection. The cutoff was five standard deviations. Figure 11a shows the processed ER dipole-dipole data with a spacing equal to 1 m. We note the sharp water-table boundary at level 5 and a strong conductive body to the left of the survey.

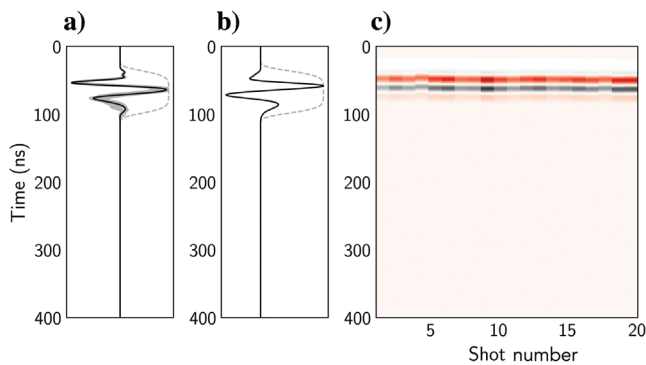


Figure 9. Results for the two stages in estimating our source wavelet. (a and b) The first stage. The shape and approximate position in time of the source wavelet in black, and the Gaussian mute in dashed gray. (a) The electric field qualitative source estimate and, in gray, the estimates for each individual shot gather. (b) The qualitative current density source wavelet. (c) The second stage showing the source wavelets for all shot gathers. Note the slight time and amplitude correction for all shot gathers. The color scale ranges from -2.7×10^6 to 4.9×10^6 A/m².

INVERSIONS

We perform three separate inversions: (1) using only the GPR data following Domenzain et al. (2020a), (2) using only the ER data following Domenzain et al. (2021), and (3) using the GPR and ER data in our joint inversion. Inversions 1 and 2 are only done to compare the recovered parameters with our joint inversions.

All of the inversions share the same discretized domain. This enables the joint inversion to accurately incorporate GPR and ER sensitivities without interpolation. Moreover, this allows GPR and ER sensitivities to directly inform the joint inversion in regions where either data coverage is weak in relation to the other.

Given the removal of short-offset GPR data, the weakest data coverage lies within the first approximately 7.5 m in length (see Figure 5). Although this region has minimal fold, it is still within the exploration

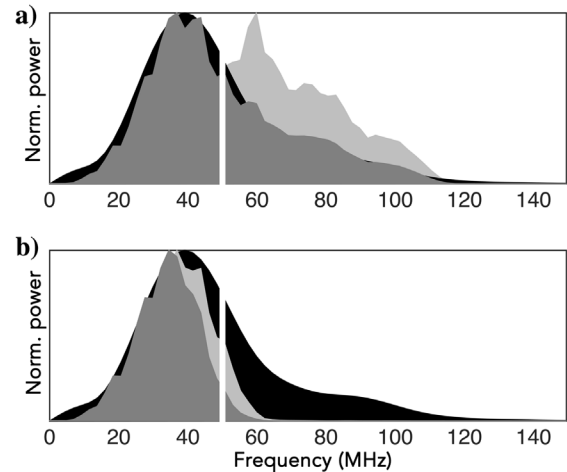


Figure 10. Power spectra of the source estimates and observed data of shot gather 1. For both panels: in black, the source estimate after stage 2 and, in light gray, using a Wiener filter with the observed data in dark gray. (a) The frequency content of the observed data band-pass filtered between 10 and 100 MHz (dark gray) yields artifacts in the recovered source (light gray and in Figure 1b in the time domain). (b) The recovered source (light gray and in Figure 1c in the time domain) is stable and has similar frequency content to the observed data band-pass filtered between 10 and 50 MHz (dark gray). Each power spectra is normalized to its own largest magnitude and is shown in linear scale.

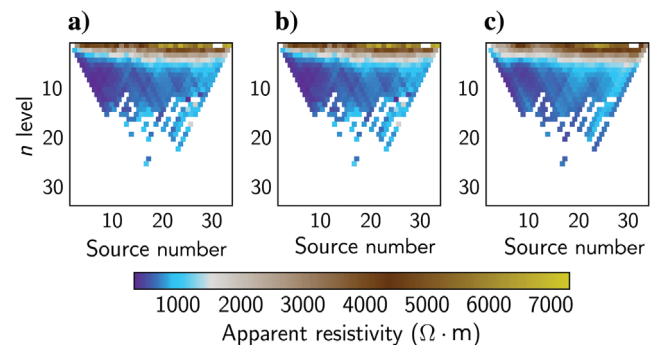


Figure 11. (a) The processed ER pseudosection for the dipole-dipole array with a spacing equal to 1 m. (b and c) The recovered pseudosection as in (a) but computed with the recovered ER and the joint inversion conductivity, respectively.

domain of the GPR data. Moreover, it is also within the solution appraisal domain given by the ER inversion alone (Domenzain et al., 2021). Therefore, we choose to present our recovered parameters within the full length of the computational domain.

All of the inversions have a homogeneous initial conductivity of 2 mS/m. This value is the average of all apparent conductivities in the data. As noted in the “Joint inversion” section, it is important for the joint inversion not to start with the conductivity solution of an ER stand-alone inversion to avoid getting trapped in a local minima for the GPR and ER objective functions. The FWI-GPR and joint inversions are initialized with a reflection tomography permittivity model (for details, see Appendix A).

At each iteration, we spatially low-pass filter each gradient for all inversions with a Gaussian filter. The widths of these filters are 0.4 and 1.6 m for the FWI-GPR and ER inversions, respectively. The envelope gradient weights for the FWI-GPR inversion are $\beta_{\epsilon} = 5 \times 10^{-3}$ and $\beta_{\sigma} = 5 \times 10^{-4}$. For the joint inversion, we use filters of width 0.5 and 1.1 m for the FWI-GPR and ER gradients, respectively. Note that we are able to decrease the smoothing on the ER gradients, while slightly increasing it for the FWI-GPR gradients. The rest of the hyperparameters for our joint inversion are found in Table 1, and their derivation is found in Appendix B.

The FWI-GPR and ER inversions were performed until just before the value of the objective functions became steadily increasing; i.e., the derivative of the objective functions with respect to the iterations was positive. We computed this with a backward finite-difference scheme on the objective function values of the last iterations. These stopping criteria are similar to Köhn et al. (2014). They compute the ratio of the last and second-to-last value and stop the inversion if this ratio is larger than a predefined positive number. For the joint inversion, we use the same number of iterations as with FWI-GPR. As detailed by Domenzain et al. (2020b), the runtime of the joint inversion is mostly dominated by FWI-GPR. Hence, our algorithm is not much more computationally expensive than the stand-alone FWI-GPR.

We evaluate the accuracy of our results by comparing them with capacitive conductivity (Mwenifumbo et al., 2009) and neutron-derived porosity (Barrash and Clemo, 2002) log data. We use Archie’s and Wyllie’s relationships (Archie, 1942; Wyllie et al., 1956) to compare the porosity data to our recovered conductivity and permittivity

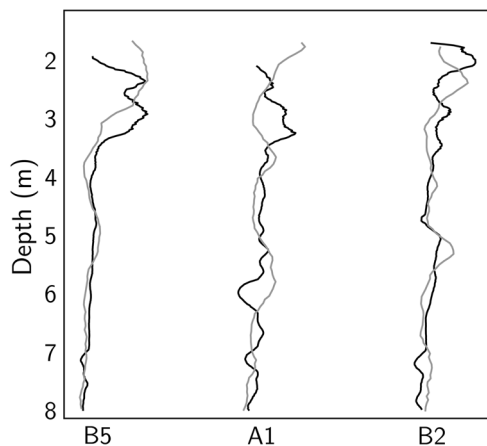


Figure 12. Normalized values of capacitive conductivity (black) and porosity (gray) for our borehole locations. Note that not all subsurface features are present in both measurements.

solutions. In the context of GPR data and assuming $\mu = \mu_o$, Wyllie’s relationship is easily shown to be equivalent to the complex refractive index method (CRIM) (Wharton et al., 1980).

Although these petrophysical relationships hold true in general, accuracy among measuring equipment can vary. Figure 12 shows the normalized values of capacitive conductivity and porosity for our borehole locations. Even though the overall trend of both measurements is similar, significant differences are present. For example, along the first 3 m, a lag is present. Below 5 m in log A1, a change in convexity is present, and below 6 m for all logs the capacitive conductivity shows more variability than porosity. On average over all logs, there is a 0.4 m lag between these data. The length of investigation was approximately 0.4 m for the porosity and capacitive conductivity (Mwenifumbo et al., 2009).

Mwenifumbo et al. (2009) find that capacitive conductivity data give a more accurate description of the subsurface than the porosity data. They do so by comparing FWI-GPR log results (Ernst et al., 2007a) that also exhibit features not present in the porosity data. Although the specific region of investigation described by Mwenifumbo et al. (2009) is located at a greater depth than our exploration domain, they suggest that contrasts in the grain size, grain-size distribution, grain shape, and/or orientation might be responsible for contrasts between the porosity and the capacitive conductivity measurements.

We remind the reader that, as explained in Appendix A, our datum $z = 0$ m is taken as the lowest topographic point in the survey, adjacent to the ground surface. Therefore, our datum lies 0.22, 0.27, and 0.4 m above in logs B5, A1, and B2, respectively, when compared with Mwenifumbo et al. (2009), Ernst et al. (2007a), Irving et al. (2007), and Bradford et al. (2009).

We find that our joint inversion recovered parameters are sensitive to an aggregate of features expressed in the capacitive conductivity and porosity log measurements.

Conductivity

Figure 13 shows the recovered conductivity for the FWI-GPR alone, ER alone, and joint inversions. In this figure and those that follow, we annotate in depth the events *a*, *b*, and *c* in the common-offset gather shown in Figure 8a. Given the weak sensitivity of the GPR data to the low conductivity at the site and our choice of initial model, the recovered conductivity is dominated by high spatial-frequency content that is not a reasonable expression of subsurface features. In contrast, the ER recovered conductivity is able to accurately find the water-table boundary (at a depth of approximately 1 m) and the water-saturated sand channel expanding inland from the left of the domain. However, the ER solution lacks high spatial-frequency content due to its inherent sensitivity to the subsurface. The joint inversion conductivity shows low- and high-spatial-frequency content. This is due to our conductivity update (see equation 12) that is able to combine the FWI-GPR and ER sensitivities in a coherent manner into our solution.

It is worth mentioning that the order of magnitude for the ER and joint recovered conductivity are in agreement with Ernst et al. (2007a), who perform 2D FWI-GPR with cross-borehole data at the same site. Although this similarity is no proof that the approximation of DC and GPR conductivities are equal, it does indicate that (at least at the BHRS) the sensitivity to the subsurface conductivity of the GPR and ER methods is in the same order of magnitude.

Figure 14 shows the capacitive and recovered ER and joint conductivity at the borehole locations. Due to the poor quality of the FWI-GPR individual recovered conductivity, we choose not to include it. Notably, all logs exhibit a more accurate shape in the joint solution above approximately 5 m. For example, the joint conductivity captures the sand channel shape between 2 and 3 m better than the ER conductivity (events *a* and *c*). Moreover, the sharp decrease in magnitude below the sand channel is also better recovered in the joint solution. At approximately 5 m in logs A1 and B2 (just above event *b*), we note that the joint solution is sensitive to the slight change in capacitive conductivity whereas the ER solution is not.

Below 5 m on all logs, the joint solution deviates from the capacitive conductivity, perhaps most notably at approximately 6 m (event *b*). For logs A1 and B2, we explain these features as porosity contrasts. Figure 14 shows the Archie-derived conductivity (in gray) using the porosity data. We assume fully saturated media, a constant cementation factor of 1.7, a fluid electrical conductivity of 20 mS/m, and a tortuosity factor of 1 following Oldenborger et al. (2007). Above 4 m for logs B5 and B2, the Archie and joint conductivity align better than the ER solution. Specifically on log B2 at a depth of approximately 2.5 m (event *c*), we see that the joint solution better matches the sharp change in porosity. This reflection event spans approximately half the length of our joint recovered conductivity, as shown in Figure 13c.

We interpret approximately 6 m contrast in log B5 (event *b*) as the continuation of the dipping horizon present on A1 and B2, and observed by Irving et al. (2007) who perform a traveltime velocity estimation of GPR crosshole data over the same boreholes. This horizon is also consistent with Ernst et al. (2007a), who perform a 2D FWI-GPR on crosshole data between logs C5 and C6 (for the borehole locations, see Figure 4a). Moreover, Bradford et al. (2009) perform a 3D ray-based tomography over the same site and find an approximately plane reflector at approximately 6 m spanning logs B1, B2, and C2. It is worth mentioning that this feature is not present in the ER solution (Figure 13b), but it is present in the joint solution (Figure 13c).

Permittivity

Figure 15 shows the initial, FWI-GPR, and joint recovered permittivity. The FWI-GPR and joint solutions show similar features that are not present in the initial model. Because the cross-gradient constraint was not present in the GPR separate inversion, the similarities between the FWI-GPR and joint solutions are expressions of only the GPR data. An example of this is the reflector spanning from log B5 at a depth of 3 m toward 36 m in length shown in Figure 15b and 15c as event *c*. The close similarity between the FWI-GPR and joint permittivity solutions is also present in synthetic examples (Domenzain et al., 2020a).

Figure 16 shows the CRIM recovered permittivity compared with our FWI-GPR, joint, and initial permittivity. We used a constant sediment permittivity of 4.6 (Clement and Barrash, 2006) and assumed a fully saturated subsurface. Qualitatively, logs B5 and A1 show a poor magnitude resolution in the shallow 2 m. However, outside this region the CRIM and recovered permittivity magnitudes are similar.

Similar to the joint recovered conductivity (Figure 13c), reflection events *a*, *b*, and *c* in the common-offset data (Figure 8a) are aligned with the reverse time migration image of the GPR data (Figure 8b). The migration image is computed with the joint recovered

parameters and overlaid with porosity and capacitive conductivity logs at the borehole locations. Most notably absent in the porosity data is the reflector at approximately 6 m in log B5 (event *b*). Similar to the joint conductivity solution (Figure 13c), the FWI-GPR

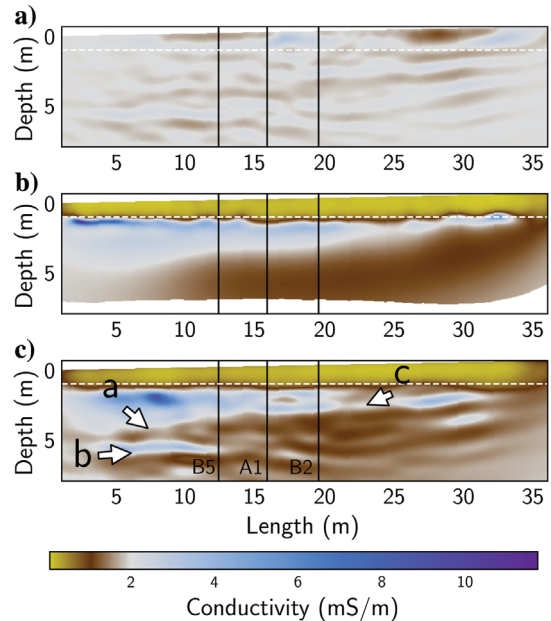


Figure 13. The (a) FWI-GPR recovered, (b) ER recovered, and (c) joint recovered conductivity. Plots are shown with topographic correction to the true incline on the BHRS. The initial conductivity was homogeneous with a value of 2 mS/m. The solid black lines mark the borehole locations, and the dashed white line marks the corrected incline of our domain relative to the flat survey datum at the location of the water-table boundary (approximately 1 m deep). The marked events *a*, *b*, and *c* correspond to the deep edge of the sand channel and reflectors at a depth of approximately 6 m and approximately 2.5 m, respectively.

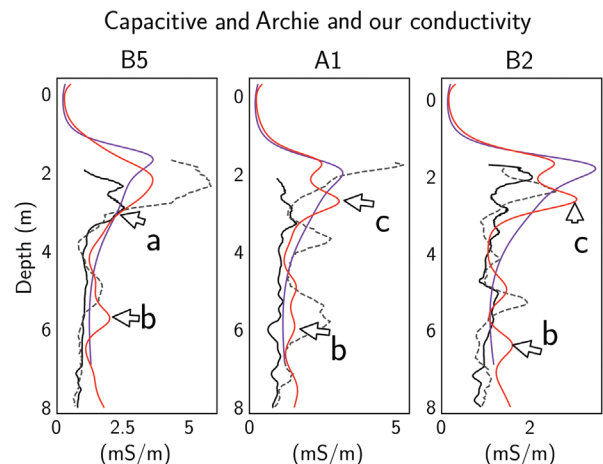


Figure 14. Log profiles of the capacitive (black), Archie (dashed gray), ER (purple), and joint conductivity (red). The initial homogeneous conductivity for the ER and joint inversions had a value of 2 mS/m. The *x*-axis has units of mS/m.

and joint permittivity find this subsurface feature (see also Figure 8b). As mentioned in the previous section, we interpret this reflector as the continuation of event *b* in log B2, which is also present in previous studies of the same site (Ernst et al., 2007a; Irving et al., 2007; Bradford et al., 2009).

Objective functions

In Figure 17a and 17b, we show the objective function values for each of our three inversions as a history of iterations. We note that the FWI-GPR and ER individual inversions reach a lower value at the final iteration. However, the FWI-GPR and ER conductivity solutions fail to capture the entirety of detail in our joint recovered conductivity (compare Figure 13a–13c). Therefore, we interpret these lower values as the result of the individual inversions converging to a local minima more quickly.

Relevant to the previous observation, we note that the FWI-GPR component of the joint inversion has a slight increase at iteration 10, and then it continues the descent at iteration 20. It is at iteration 10 that the joint inversion overcomes the local minima where the individual FWI-GPR inversion converges. Notably, the joint inversion is capable of overcoming the nonlinearity of the solution space. We accomplish this by letting the ER sensitivity guide the conductivity solution. As shown in Figure 17c, after iteration 10, the values of the joint sensitivity weights are strongly biased (more than 50%) toward the ER conductivity update.

Qualitatively, the weights in Figure 17c and 17d follow the shapes shown in Figure 2. At early iterations a_w dominates, whereas at late iterations this role is smoothly reversed toward a_{dc} . In the

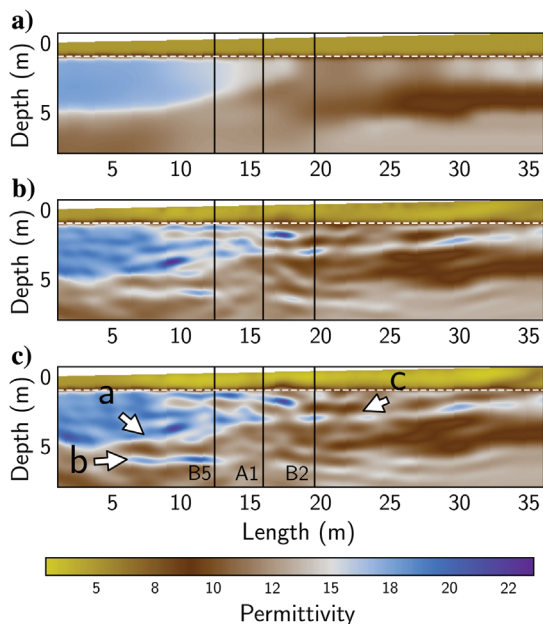


Figure 15. (a) Initial, (b) FWI-GPR recovered, and (c) joint recovered electrical permittivity. Plots are shown with topographic correction to the true incline on the BHRS. The solid black lines mark the borehole locations, and the dashed white line marks the corrected incline of our domain relative to the flat survey datum at the location of the water-table boundary (approximately 1 m deep). The marked events *a*, *b*, and *c* correspond to the deep edge of the sand channel and reflectors at approximately 6 m and approximately 2.5 m deep, respectively.

case of β_σ and β_{ϵ_r} , at early iterations their values are small, and at late iterations their final asymptotic values are reached when a_{dc} no longer contributes to the inversion (i.e., when a_w reaches its asymptotic value).

We find that for this data set, the envelope and cross-gradient weights do not contribute much difference to the inversion. However, nonzero values regularize the inversion allowing for a smaller final value of Θ .

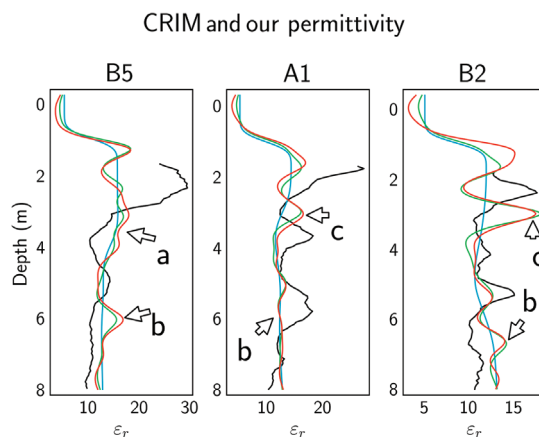


Figure 16. Log profiles of the electrical permittivity computed with porosity and the CRIM relation (black), initial (blue), FWI-GPR recovered (green), and joint recovered (red). The x -axis has units of relative permittivity (unitless).

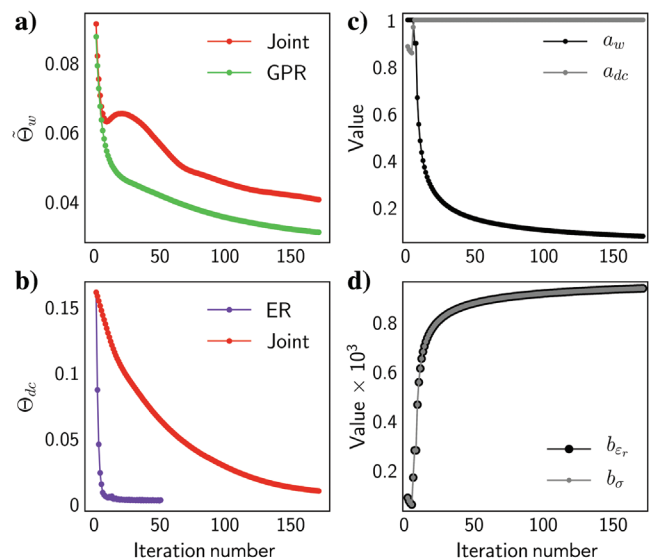


Figure 17. (a and b) The history of the objective function values for our inversions. (a) The FWI-GPR (green) and the FWI-GPR component of the joint (red). (b) The ER (purple) and the ER component of the joint (red). (c and d) The value of the joint inversion weights at each iteration. (c) The weights for joining the FWI-GPR and ER conductivity updates. (d) The weights for joining the cross-gradient updates. The values for the FWI-GPR envelope weight are kept constant at $\beta_{\epsilon_r} = 5 \times 10^{-3}$ and $\beta_\sigma = 10^{-3}$.

Recovered data

Figures 6d and 11c show examples of the FWI-GPR and ER data computed with our joint recovered parameters (shown in Figure 15c for permittivity and in Figure 13c for conductivity). In the case of the GPR data, we choose to show shot gather 1, which spans most of the exploration domain (see Figure 5) and thus holds information of all the discussed events.

Figure 6c shows the FWI-GPR data computed with the initial models. Comparing Figure 6b–6d, we find many features in the recovered data that are not present in the initial data; for example, at long offsets, the early linear arrival is more accurately recovered in Figure 6d than 6c. The quality enhancement is also present at short offsets and at greater than approximately 250 ns. At less than 250 ns, our recovered data struggle to accurately resolve the reflection events present in the observed data.

However, when compared with the GPR stand-alone inversion (see Figure 18a), our joint recovered data do not exhibit cycle skipping because the GPR stand-alone inversion does for this shot gather. This is notably evident between approximately 13–17 m and 300–350 ns in Figure 18a. This cycle-skipping behavior is only apparent after a cubic gain in time. Without gain, we show in Figure 18b the first GPR trace of shot gather 1 computed with our initial, FWI-GPR, and joint recovered parameters. This receiver is directly above event *b*. The FWI-GPR and joint recovered data are very similar. This is to be expected given the close rms value of their objective functions (see Figure 17a). Specifically, at approximately 220 ns, we note that the joint recovered data have better low-frequency content than the FWI-GPR recovered data. The cycles that were not skipped and the improved low-frequency content are the result of the ER data enhancing the recovered parameters.

In Figure 11b, we show the ER recovered data using the ER recovered conductivity (Figure 13b). The fit to the observed data is better with the ER solution (see also Figure 17b). However, the joint recovered ER data show smoother apparent resistivity values, for example, at shallow *n* levels along the 7000–1000 $\Omega \cdot \text{m}$ interface and at *n* levels 15–25.

DISCUSSION

Our algorithm is able to recover subsurface electrical parameters using only GPR and ER surface-acquired data. In contrast with recent work on GPR surface-acquired inversion techniques that use the full waveform of the data (e.g., Busch et al., 2012; Liu et al., 2018), we make explicit use of the adjoint method to compute the GPR and ER sensitivities. This enables us to make no assumptions about the underlying subsurface geometry, i.e., whether it is layered or a known shape located in a homogeneous half-space.

An important limitation of our method (which is present in all FWI literature) is the need for a good initial velocity model. In this case, we used an existing reflection-tomography velocity model from a different GPR data set acquired in a different year (for details, see Appendix A).

We assume that DC and GPR conductivity are approximately equal. Although this is not true in general, we find that, with these field data, this approximation is accurate. This may be because the sensitivity of GPR to relaxation mechanisms in the subsurface is weak (in this case) and is therefore not apparent in the data. Because this is not always the case, future research is needed to address this issue.

The joint inversion recovered parameters (Figures 13c and 15c) show a combination of features present in the porosity and capacitive conductivity log measurements (Barrash and Clemo, 2002; Mwenifumbo et al., 2009). Given the different sensitivities of these log measurements, not all subsurface features are present in both data sets (see Figure 12). Based on the previous GPR cross-borehole and 3D surface-acquired surveys at the same site (Ernst et al., 2007a; Irving et al., 2007; Bradford et al., 2009), we are confident that our joint recovered parameters correctly resolve the reflector at a depth of approximately 6 m. Notably, this reflector is missing from some log porosity and capacitive conductivity measurements, and it is not recovered by ER data alone.

Although the FWI-GPR and joint recovered permittivity have a close resemblance, the FWI-GPR solution for conductivity is of low quality in magnitude and spatial frequency content. Furthermore, the FWI-GPR permittivity lacks the resolution of the approximately 6 m deep reflector compared to the joint inversion permittivity. Notably, this short-wavelength anomaly is also missing in the ER conductivity solution but is present in the joint recovered conductivity.

We examine the quality of our results with respect to our control log data in Figure 19. We perform an average over all logs of the maximum crosscorrelation value and the absolute lag at which this maximum value was found. These average values include crosscorrelation results of porosity and capacitive conductivity, and they are computed only with the crosscorrelations that are comparable in our separate inversions. The values of all crosscorrelation averages are normalized by the average value over all logs of porosity crosscorrelated with capacitive conductivity. This specific crosscorrelation is marked with a solid star in Figure 19. We interpret any value to the left of the solid star as a gain in recovered subsurface structure with respect to our control data. The *y*-axis values in Figure 19 are interpreted as a measure of quality of the recovered subsurface structure.

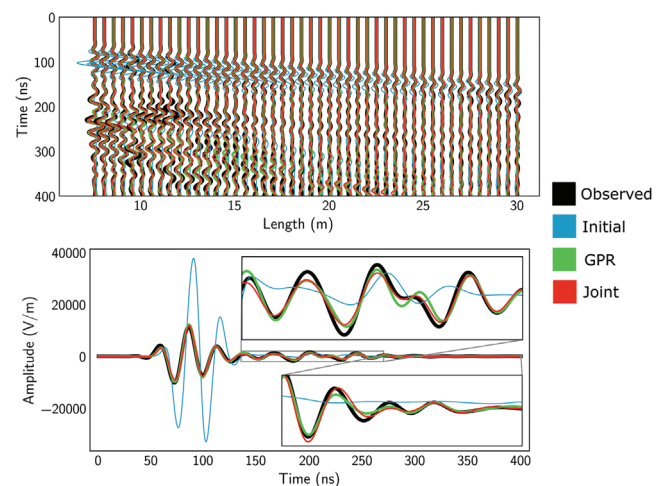


Figure 18. (a and b) The GPR data computed with the initial models in thin blue, with the FWI-GPR recovered parameters in thick green and the joint recovered parameters in thin red. The observed data are shown in thick black. (a) The GPR shot gather 1 gained in time by t^3 . (a) The first trace of shot gather 1 (at approximately 7 m in length and above event *b*) with no gain applied. The top and bottom subpanels of (b) are magnified to ± 2000 and ± 400 V/m, respectively. The time interval for the top subpanel is 135–270 ns, whereas for the bottom subpanel is 270–400 ns.

Comparing our separate GPR and ER inversions with our joint inversion results (Figure 19), we find that our joint inversion outperforms the individual inversions with respect to the control data. Notably, the joint conductivity solution averages a smaller spatial lag (0.1 versus 0.4 m) and larger crosscorrelation value (at 110%) than the control data. Although the GPR recovered parameters have a smaller spatial lag than the control data (0.3 versus 0.4 m), the maximum value of the crosscorrelation is only 80% that of the control data.

Domenzain et al. (2020a) perform a synthetic joint FWI-GPR and ER surface-acquired data inversion on a subsurface scenario similar to the field case presented here. Mainly, their synthetic model has a dry shallow layer followed by a water-saturated region, which loosely resembles the sand channel shape found in the BHRS. Relevant to our discussion here, Domenzain et al. (2020a) compare inversion results with varying initial models that differ in permittivity values and position of the first shallow layer. They show that, without precise knowledge of the shallow layer, the GPR data cannot accurately recover the sharp dry/water-saturated contrast. Moreover, when the initial permittivity lacks perfect resolution in the first layer, the water-saturated region is recovered at depth with a peak-valley-peak shape. This shape is reminiscent of that in Figure 16 on log B5 between approximately 1.5 m and approximately 3 m in depth. Therefore, we attribute the lack of our recovered permittivity resolution in this shallow region to our initial model.

The joint inversion rms values for FWI-GPR and ER data are greater than those of individual inversions (see Figure 17a and 17b). However, FWI-GPR converges to a poor conductivity solution and the ER conductivity lacks spatial-frequency content found in log measurements. Therefore, we interpret the lower values of the individual inversions as convergence to local minima. Figure 17a shows how the joint inversion FWI-GPR objective function

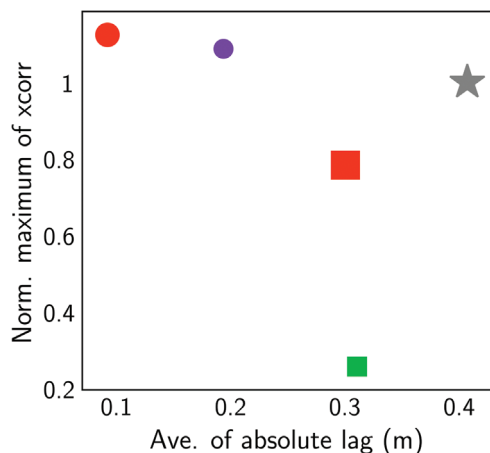


Figure 19. Comparison of averages over all boreholes of maximum crosscorrelation values (and their respective spatial lags) of our recovered parameters with log data. The maximum crosscorrelation values are normalized by the value of porosity crosscorrelated with capacitive conductivity, which is denoted by a solid star. The averages of porosity and capacitive conductivity crosscorrelated with the ER recovered conductivity (the purple circle), the joint recovered conductivity (the red circle), the FWI-GPR recovered parameters (the green square), and the joint recovered parameters (the red square). Smaller values on the x -axis and larger values on the y -axis are better.

is able to avoid convergence to local minima (between iterations 10 and 20) while being guided by the ER sensitivity (see Figure 17b and 17c).

The hyperparameters (see Table 1) needed in our joint inversion took three inversion runs to determine (for details, see Appendix B). We note that these hyperparameters depend only on the data and the initial models. Once the steps outlined in Appendix B have been fulfilled, changing the hyperparameters does not drastically change the recovered models.

The GPR data computed with the joint recovered parameters are similar to those of the FWI-GPR solution. However, some reflections in the GPR joint recovered data have more accurate low-frequency content, whereas some sections of the data do not exhibit cycle skipping like the FWI-GPR stand-alone inversion does (see Figure 18). The ER data computed with the ER conductivity solution are a more accurate fit to the observed data (see Figure 11b). However, the joint solution fits the log data more accurately. We conclude that features in the observed ER data not present in the ER joint recovered data are the result of the inherent limitations of the ER method rather than the subsurface expressions.

CONCLUSION

We have presented the results of a joint multiphysics, multiparameter inversion of FWI-GPR and ER field data acquired on the surface. Our joint inversion scheme simultaneously solves for subsurface permittivity and conductivity by using the GPR and ER sensitivities at each iteration. This means that we do not use either the GPR or ER recovered conductivity as reference models in the inversion. Moreover, the FWI-GPR and ER sensitivities are computed on the same discretized domain. Hence, we do not interpolate between the ER and GPR forward model domains. The source estimation routine is embedded within the FWI-GPR and joint inversion. Frequency content conditions for the GPR data are explained in order for the source estimation to be stable. Our method does not invoke petrophysical relationships. However, we compare our results to existing log measurements of neutron-derived porosity and capacity conductivity data.

We present our algorithm in a 2.5D domain. This subsurface approximation is accurate based on previous work at the same site. Our scheme can be extended to three dimensions by modifying the forward models, although the computational burden would significantly increase.

We choose to show our method specifically on surface-acquired data because of the challenging conditions this configuration imposes on the inverse problem — mainly the lack of transmission data. However, we note that our method can be applied to borehole GPR. In the case of ER borehole data, boundary conditions in the 2.5D forward model (and in the sensitivity computations) would have to be modified accordingly.

The field site is a controlled alluvial aquifer that exhibits a shallow water table boundary and unconsolidated heterogeneous alluvial deposits. We assess our method by performing the FWI-GPR and ER individual inversions. Our joint inversion outperforms both individual inversions for permittivity and conductivity. The FWI-GPR recovered conductivity gives a very poor result. Although the data fit for the ER recovered conductivity is better than that of the joint inversion result, the ER solution overfits the data, whereas the joint recovered solution more closely resembles log measurements. The FWI-GPR alone recovered permittivity gives a result close to the joint inversion

solution. However, subsurface features at depth present in log measurements and in previous studies are more accurately resolved by the joint permittivity solution.

DATA AND MATERIALS AVAILABILITY

Data associated with this research are available and can be obtained by contacting the corresponding author.

APPENDIX A

GPR INITIAL VELOCITY MODEL

The initial velocity model in our inversion was taken from a ray-based tomography of a previous survey, which consisted of multi-offset GPR data acquired on the ground surface with 50 and 100 MHz antennae. The survey line coincided with ours, but the survey was done at a different time of the year when the water table was at a depth of approximately 2 m. The velocity inversion was done using prestack depth migration following Bradford (2006). A field application of this method on the same site (BHRS) over the same survey line is presented by Bradford et al. (2009). We transform the velocity values v to relative permittivity ϵ_r by assuming magnetic permeability equal to that of free space, i.e., $\epsilon_r = (c/v)^2$,

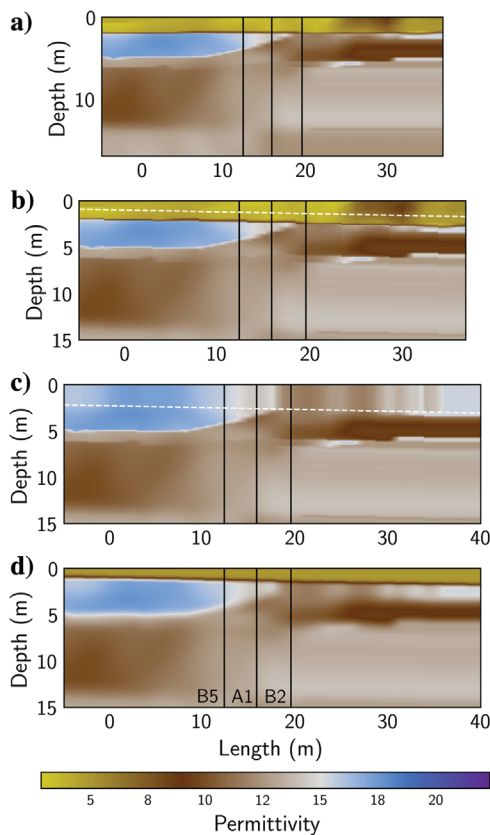


Figure A-1. Different stages in building our initial permittivity. (a) As given by the ray-based tomography. (b) With topographic correction applied. (c) After removing the first layer. (d) The permittivity model after smoothing, ready for the joint inversion. The log locations are marked in black, and in white are the selected horizons used for editing. All figures are shown with a one-to-one aspect ratio.

where c is the speed of light. Figure A-1a shows the section of the ray-based velocity model before any necessary corrections for the joint inversion.

We now explain the corrections made to the permittivity model obtained by the ray-based tomography. Because the model shown in Figure A-1a was computed using a flat datum, our first step is to correct for topography. Our datum matches $z = 0$ m to the lowest point on the ground surface. The $z = 0$ m level curve is adjacent (not parallel) to the ground surface. Given that our computational domain is a Cartesian rectangle, we fill the missing values after the topographic correction by averaging neighboring cells. Figure A-1b shows the permittivity model after these two steps. Also in Figure A-1b, we show the boundary between the first layer and the ground-water table in white. This boundary coincides with the ER conductivity inversion alone (Figure 13b) and onsite log measurements to the water-table depth. Values above this boundary averaged a permittivity value of five.

Because the ray-based permittivity model does not span the full extent of length in our domain, we add 4 m by repeating the last column in Figure A-1b. We also crop the lower part of the model to comply with our 15 m deep domain. The next step is to spatially interpolate from the current $\Delta x = 0.25$ m and $\Delta z = 0.1$ m to our domain $\Delta x = \Delta z = 0.05$ m. Once interpolated, we remove the approximately 2 m deep first layer of the ray-based permittivity by repeating the values along the white boundary in Figure A-1c. We now smooth the entire domain with a low-pass Gaussian filter in the spatial-frequency domain of 2 m width. We choose the width of the Gaussian filter to visually remove artifacts due to the topographic correction, interpolation, and sharp horizons found during the ray-based tomography.

We now introduce the approximately 1 m deep first layer with the previously found average permittivity value of five. This step changes the values above the white boundary in Figure A-1b. Then, we smooth the entire domain again, but this time using a Gaussian low-pass filter of width of 1.3 m. The different choice in width of the Gaussian filters (2 and 1.3 m) was made following Domenzain et al. (2020a), where it is synthetically shown that sharp first-layer boundaries greatly improve the quality of the recovered parameters.

APPENDIX B

FINDING THE JOINT INVERSION HYPERPARAMETERS

We find the hyperparameters used in the joint inversion (see Table 1) by first finding the parameters that determine Figure 2a and then those that determine Figure 2b. Our approach requires a small number of joint inversions. We refer to each such inversion as an *inversion run*. Our choosing criteria are based on the final value of the objective function of each inversion run.

In what follows, we assume individual FWI-GPR and ER inversions have been performed and have yielded satisfactory results, i.e., the rms values of the objective functions decrease through iterations, and the recovered parameters do not exhibit nonphysical artifacts. In the case of GPR FWI, this entails having a good initial velocity model and a stable source estimation scheme.

The most dominant parameters that determine Figure 2a are a_{dc} , \hat{a}_{dc} , \hat{a}_w , $\hat{\Theta}_{dc}$, and $\hat{\Theta}_{w,\sigma}$ (in that order). At this stage, we set the parameters of Figure 2b (d_e , h_e , d_σ , h_σ , β_e , β_σ) equal to

Table B-1. Strategy for finding the hyperparameter values in our joint inversion scheme.

Weight	Run 1	Run 2	Run 3
a_{dc}	0.5	0.9	0.9
\dot{a}_{dc}	2	2	2
$\dot{\Theta}_{dc}$	4	4	4
\dot{a}_w	5	5	10
$\dot{\Theta}_{w,\sigma}$	0.9	0.9	0.9

The boxed numbers mark a desirable change with respect to the last inversion run.

zero. First, we try a value of $a_{dc} = 0.5$ and then a value of $a_{dc} = 0.9$, which yields a smaller objective function value. Because $a_{dc} = 0.9$ is already close to one, we choose not to increase \dot{a}_{dc} and leave it fixed at two. Then, we increase the value of \dot{a}_w to 10. This, again, yields a smaller objective function value. This choice of parameters gives a stable joint inversion and acceptable results, and in Table B-1 we show a condensed view of this procedure. In general, for every inversion run considered, the weights a_w and a_{dc} should qualitatively follow the shape in Figure 2a. If this is not the case, we recommend tuning \dot{a}_{dc} first, and then \dot{a}_w until such a shape is achieved.

We now find the parameters for Figure 2b: $\beta_{e_r}, \beta_{\sigma}, d_{e_r}, h_{e_r}, d_{\sigma}$, and h_{σ} . For this data set, these values had little influence in the inversion. We choose these values as shown in Table 1. In general, we recommend values of this order of magnitude for these hyperparameters. For this data set, small variations in these values did not affect the inversion results in a relevant way.

REFERENCES

- Annan, A. P., 1996, Transmission dispersion and GPR: *Journal of Environmental and Engineering Geophysics*, **1**, 125–136, doi: [10.4133/JEEG1.B.125](https://doi.org/10.4133/JEEG1.B.125).
- Archie, G. E., 1942, The electrical resistivity log as an aid in determining some reservoir characteristics: *Transactions of the AIME*, **146**, 54–62, doi: [10.2118/942054-G](https://doi.org/10.2118/942054-G).
- Babcock, E., and J. H. Bradford, 2015, Reflection waveform inversion of ground-penetrating radar data for characterizing thin and ultrathin layers of nonaqueous phase liquid contaminants in stratified media: *Geophysics*, **80**, no. 2, H1–H11, doi: [10.1190/geo2014-0037.1](https://doi.org/10.1190/geo2014-0037.1).
- Barrash, W., and T. Clemo, 2002, Hierarchical geostatistics and multifacies systems: Boise Hydrogeophysical Research Site, Boise, Idaho: *Water Resources Research*, **38**, 14-1, doi: [10.1029/2002WR001436](https://doi.org/10.1029/2002WR001436).
- Barrash, W., T. Clemo, and M. D. Knoll, 1999, Boise Hydrogeophysical Research Site (BHRS): Objectives, design, initial geostatistical results: *Symposium on the Application of Geophysics to Engineering and Environmental Problems*, 389–398.
- Barrash, W., and E. C. Reboulet, 2004, Significance of porosity for stratigraphy and textural composition in subsurface, coarse fluvial deposits: Boise Hydrogeophysical Research Site: *Geological Society of America Bulletin*, **116**, 1059–1073, doi: [10.1130/B25370.1](https://doi.org/10.1130/B25370.1).
- Beff, L., T. Gunther, B. Vandoorne, V. Couvreur, and M. Javaux, 2013, Three-dimensional monitoring of soil water content in a maize field using electrical resistivity tomography: *Hydrology and Earth System Sciences*, **17**, 595–609, doi: [10.5194/hess-17-595-2013](https://doi.org/10.5194/hess-17-595-2013).
- Bleistein, N., 1986, Two-and-one-half dimensional in-plane wave propagation: *Geophysical Prospecting*, **34**, 686–703, doi: [10.1111/j.1365-2478.1986.tb00488.x](https://doi.org/10.1111/j.1365-2478.1986.tb00488.x).
- Bradford, J. H., 2006, Applying reflection tomography in the postmigration domain to multifold ground-penetrating radar data: *Geophysics*, **71**, no. 1, K1–K8, doi: [10.1190/1.2159051](https://doi.org/10.1190/1.2159051).
- Bradford, J. H., 2012, GPR prestack amplitude recovery for radiation patterns using a full wave-equation, reverse-time migration algorithm: 82nd Annual International Meeting, SEG, Expanded Abstracts, doi: [10.1190/segam2012-1444.1](https://doi.org/10.1190/segam2012-1444.1).
- Bradford, J. H., W. P. Clement, and W. Barrash, 2009, Estimating porosity with ground-penetrating radar reflection tomography: A controlled 3D experiment at the Boise Hydrogeophysical Research Site: *Water Resources Research*, **45**, W00D26, doi: [10.1029/2008WR006960](https://doi.org/10.1029/2008WR006960).
- Busch, S., J. van der Kruk, J. Bikowski, and H. Vereecken, 2012, Quantitative conductivity and permittivity estimation using full-waveform inversion of on-ground GPR data: *Geophysics*, **77**, no. 6, H79–H91, doi: [10.1190/geo2012-0045.1](https://doi.org/10.1190/geo2012-0045.1).
- Carrigan, C. R., X. Yang, D. J. LaBrecque, D. Larsen, D. Freeman, A. L. Ramirez, W. Daily, R. Aines, R. Newmark, J. Friedmann, and S. Hovorka, 2013, Electrical resistance tomographic monitoring of CO₂ movement in deep geologic reservoirs: *International Journal of Greenhouse Gas Control*, **18**, 401–408, doi: [10.1016/j.ijggc.2013.04.016](https://doi.org/10.1016/j.ijggc.2013.04.016).
- Clement, W. P., and W. Barrash, 2006, Crosshole radar tomography in a fluvial aquifer near Boise, Idaho: *Journal of Environmental and Engineering Geophysics*, **11**, 171–184, doi: [10.2113/JEEG11.3.171](https://doi.org/10.2113/JEEG11.3.171).
- Courant, R., K. Friedrichs, and H. Lewy, 1967, On the partial difference equations of mathematical physics: *IBM Journal of Research and Development*, **11**, 215–234, doi: [10.1147/rd.112.0215](https://doi.org/10.1147/rd.112.0215).
- Domenzain, D., J. Bradford, and J. Mead, 2020a, Joint inversion of full-waveform GPR and ER data — Part 2: Enhancing low frequencies with the envelope transform and cross-gradients: *Geophysics*, **85**, no. 6, H115–H132, doi: [10.1190/geo2019-0755.1](https://doi.org/10.1190/geo2019-0755.1).
- Domenzain, D., J. Bradford, and J. Mead, 2020b, Joint inversion of full-waveform ground-penetrating radar and electrical resistivity data — Part 1: *Geophysics*, **85**, no. 6, H97–H113, doi: [10.1190/geo2019-0754.1](https://doi.org/10.1190/geo2019-0754.1).
- Domenzain, D., J. Bradford, and J. Mead, 2021, Efficient inversion of 2.5D electrical resistivity data using the discrete adjoint method: *Geophysics*, **86**, no. 3, E225–E237, doi: [10.1190/geo2020-0373.1](https://doi.org/10.1190/geo2020-0373.1).
- Ernst, J. R., A. G. Green, H. Maurer, and K. Holliger, 2007a, Application of a new 2D time-domain full-waveform inversion scheme to crosshole radar data: *Geophysics*, **72**, no. 5, J53–J64, doi: [10.1190/1.2761848](https://doi.org/10.1190/1.2761848).
- Ernst, J. R., H. Maurer, A. G. Green, and K. Holliger, 2007b, Full-waveform inversion of crosshole radar data based on 2D finite-difference time-domain solutions of Maxwell's equations: *IEEE Transactions on Geoscience and Remote Sensing*, **45**, 2807–2828, doi: [10.1109/TGRS.2007.901048](https://doi.org/10.1109/TGRS.2007.901048).
- Groos, L., M. Schafer, T. Forbriger, and T. Bohlen, 2017, Application of a complete workflow for 2D elastic full-waveform inversion to recorded shallow-seismic Rayleigh waves workflow for FWI of Rayleigh waves: *Geophysics*, **82**, no. 2, R109–R117, doi: [10.1190/geo2016-0284.1](https://doi.org/10.1190/geo2016-0284.1).
- Irving, J. D., M. D. Knoll, and R. J. Knight, 2007, Improving crosshole radar velocity tomograms: A new approach to incorporating high-angle travel-time data: *Geophysics*, **72**, no. 4, J31–J41, doi: [10.1190/1.2742813](https://doi.org/10.1190/1.2742813).
- Kaufmann, M. S., A. Klotzsche, H. Vereecken, and J. van der Kruk, 2020, Simultaneous multichannel multi-offset ground-penetrating radar measurements for soil characterization: *Vadose Zone Journal*, **19**, e20017, doi: [10.1002/vzj2.20017](https://doi.org/10.1002/vzj2.20017).
- Klotzsche, A., J. van der Kruk, J. Bradford, and H. Vereecken, 2014, Detection of spatially limited high-porosity layers using crosshole GPR signal analysis and full-waveform inversion: *Water Resources Research*, **50**, 6966–6985, doi: [10.1002/2013WR015177](https://doi.org/10.1002/2013WR015177).
- Klotzsche, A., H. Vereecken, and J. van der Kruk, 2019, Review of crosshole ground-penetrating radar full-waveform inversion of experimental data: Recent developments, challenges, and pitfalls: *Geophysics*, **84**, no. 6, H13–H28, doi: [10.1190/geo2018-0597.1](https://doi.org/10.1190/geo2018-0597.1).
- Köhn, D., D. De Nil, A. Kurzmann, A. Przebindowska, and T. Bohlen, 2012, On the influence of model parametrization in elastic full waveform tomography: *Geophysical Journal International*, **191**, no. 1, 325–345, doi: [10.1111/j.1365-246x.2012.05633.x](https://doi.org/10.1111/j.1365-246x.2012.05633.x).
- Liu, T., A. Klotzsche, M. Pondkule, H. Vereecken, Y. Su, and J. van der Kruk, 2018, Radius estimation of subsurface cylindrical objects from ground-penetrating-radar data using full-waveform inversion: *Geophysics*, **83**, no. 6, H43–H54, doi: [10.1190/geo2017-0815.1](https://doi.org/10.1190/geo2017-0815.1).
- Meles, G., S. Greenhalgh, J. Van der Kruk, A. Green, and H. Maurer, 2012, Taming the non-linearity problem in GPR full-waveform inversion for high contrast media: *Journal of Applied Geophysics*, **78**, 31–43, doi: [10.1016/j.jappgeo.2011.12.001](https://doi.org/10.1016/j.jappgeo.2011.12.001).
- Meles, G. A., J. Van der Kruk, S. A. Greenhalgh, J. R. Ernst, H. Maurer, and A. G. Green, 2010, A new vector waveform inversion algorithm for simultaneous updating of conductivity and permittivity parameters from combination crosshole/borehole-to-surface GPR data: *IEEE Transactions on Geoscience and Remote Sensing*, **48**, 3391–3407, doi: [10.1109/TGRS.2010.2046670](https://doi.org/10.1109/TGRS.2010.2046670).
- Mozaffari, A., A. Klotzsche, C. Warren, G. He, A. Giannopoulos, H. Vereecken, and J. van der Kruk, 2020, 2.5 D crosshole GPR full-waveform inversion with synthetic and measured data: *Geophysics*, **85**, no. 4, H71–H82, doi: [10.1190/geo2019-0600.1](https://doi.org/10.1190/geo2019-0600.1).
- Mwenifumbo, C. J., W. Barrash, and M. D. Knoll, 2009, Capacitive conductivity logging and electrical stratigraphy in a high-resistivity

- aquifer, Boise Hydrogeophysical Research Site: *Geophysics*, **74**, no. 3, E125–E133, doi: [10.1190/1.3106760](https://doi.org/10.1190/1.3106760).
- Oldenborger, G. A., M. D. Knoll, P. S. Routh, and D. J. LaBrecque, 2007, Time-lapse ERT monitoring of an injection/withdrawal experiment in a shallow unconfined aquifer: *Geophysics*, **72**, no. 4, F177–F187, doi: [10.1190/1.2734365](https://doi.org/10.1190/1.2734365).
- Parsekian, A. D., L. Slater, and D. Gimenez, 2012, Application of ground-penetrating radar to measure near-saturation soil water content in peat soils: *Water Resources Research*, **48**, W02533, doi: [10.1029/2011WR011303](https://doi.org/10.1029/2011WR011303).
- Pratt, R. G., C. Shin, and G. Hick, 1998, Gauss-Newton and full Newton methods in frequency-space seismic waveform inversion: *Geophysical Journal International*, **133**, 341–362, doi: [10.1046/j.1365-246X.1998.00498.x](https://doi.org/10.1046/j.1365-246X.1998.00498.x).
- Spichak, V. V., and O. K. Zakharova, 2015, *Electromagnetic geothermometry*: Elsevier.
- Tarantola, A., 1984, Inversion of seismic reflection data in the acoustic approximation: *Geophysics*, **49**, 1259–1266, doi: [10.1190/1.1441754](https://doi.org/10.1190/1.1441754).
- Virieux, J., and S. Operto, 2009, An overview of full-waveform inversion in exploration geophysics: *Geophysics*, **74**, no. 6, WCC1–WCC26, doi: [10.1190/1.3238367](https://doi.org/10.1190/1.3238367).
- Wharton, R. P., R. N. Rau, and D. L. Best, 1980, *Electromagnetic propagation logging: Advances in technique and interpretation*: Presented at the SPE Annual Technical Conference and Exhibition.
- Wyllie, M. R. J., A. R. Gregory, and L. W. Gardner, 1956, Elastic wave velocities in heterogeneous and porous media: *Geophysics*, **21**, 41–70, doi: [10.1190/1.1438217](https://doi.org/10.1190/1.1438217).

Biographies and photographs of the authors are not available.